Powder-Route Synthesis and Mechanical Testing of Ultrafine Grain Tungsten Alloys

Citation: Cordero, Zachary C. et al. "Powder-Route Synthesis and Mechanical Testing of Ultrafine Grain Tungsten Alloys." Metallurgical and Materials Transactions A 45.8 (2014): 3609–3618.

As Published: http://dx.doi.org/10.1007/s11661-014-2286-1

Publisher: Springer US

Persistent URL: http://hdl.handle.net/1721.1/103306

Version: Author's final manuscript: final author's manuscript post peer review, without publisher's formatting or copy editing

Manuscript submitted November 6, 2013.

Powder-Route Synthesis and Mechanical Testing of Ultrafine Grain Tungsten Alloys

Zachary C. Cordero[1], Emily L. Huskins[2], Mansoo Park[1], Steven Livers[3], Megan Frary[3], Brian E. Schuster[4], Christopher A. Schuh[1]

1. Department of Materials Science and Engineering, MIT, Cambridge MA 02139
2. Oak Ridge Institute for Science and Education Postdoctoral Fellowship Program, Army Research Laboratory, Aberdeen Proving Ground MD 21005
3. Department of Materials Science & Engineering, Boise State University, Boise ID 83725
4. Weapons and Materials Research Directorate, Army Research Laboratory, Aberdeen Proving Ground MD 21005

We report a W-rich alloy (W-7Cr-9Fe, at%) produced by high energy ball milling, with alloying additions that both lower the densification temperature and retard grain growth. The alloy's consolidation behavior and the resultant compacts' microstructure and mechanical properties are explored. Under one condition, a 98% dense compact with a mean grain size of 130 nm was achieved, and exhibited a hardness of 13.5 GPa, a dynamic uniaxial yield strength of 4.14 GPa in Kolsky bar experiments, and signs of structural shear localization during deformation.

I. Introduction

Ultrafine grain tungsten's high density, compressive strength, and propensity for shear banding make it an attractive material for penetration applications, although the amount of available data supporting its unique mechanical properties remains limited due to processing constraints.[1,2] One major constraint has been the limited dimensions of W specimens whose grain sizes are refined by severe plastic deformation techniques such as wire drawing and high pressure torsion.[3–7] For example, Wei and coworkers used high pressure torsion to prepare a W specimen whose grain size was refined to about 170 nm, but this technique is limited to specimen geometries of ~1 mm thickness and ~10 mm diameter.[7,8] Much higher aspect ratio specimens are required for traditional ballistic testing.[9] Furthermore, severe plastic deformation techniques (e.g., cold rolling and equal channel angular extrusion) are capable of yielding larger specimens, but generally have produced W specimens with coarser ultimate grain sizes (>500 nm).[6,10,11] It is thus of interest to synthesize ultrafine grain W specimens using more readily scalable methods, for example based on powder processing.

Previous efforts to synthesize ultrafine grain W articles using powder processing have generally found that pressure-assisted sintering and alloying are necessary for achieving high relative densities without grain growth.[6,12–19] Hot isostatic pressing, for example, was used to consolidate 50 nm W particles to >95% relative density between 1093 and 1193 K (820 and 920 °C).[20] Because these temperatures are below the grain growth onset temperature of unalloyed tungsten (1273-1373 K (1000-1100 °C)), grain growth was suppressed, and the compacts retained grain sizes as small as 150 nm.[21] Attempts

to replicate these results using other pressure-assisted sintering techniques such as field assisted sintering (FAS) used lower stresses; whereas the hot isostatic pressing study used an isostatic pressure of 1 GPa, the maximum uniaxial stress reported in FAS studies is 266 MPa.[6,16–19] Consequently, these FAS studies generally required higher soak temperatures (>1273 K (1000 °C)) or longer hold times to achieve similar relative densities. Despite FAS's fast ramp rates, the higher thermal excursion led to coarse (>1 μm) grains and commensurately degraded mechanical properties. Hence, pressure-assisted sintering and rapid ramp rates, although beneficial, cannot guarantee low porosity and ultrafine grains.

In addition to merely increasing consolidation pressure and thermal excursion, it is also desirable to consider W alloys containing elements that accelerate densification at lower temperatures and/or retard grain growth, thereby decreasing the necessary soak temperature and allowing longer hold times at higher temperatures. This, in turn, can reduce the need for very high consolidation pressures. Accordingly, this approach is taken in the present work, in which we describe a specific nanocrystalline, W-based alloy powder (W-7Cr-9Fe, at%) that can consolidate to high relative densities without excessive grain growth during FAS. Two-phase, ultrafine grain compacts made from the powder exhibit high hardness and dynamic compressive strengths, as well as a tendency to shear localize. Examination of the structure and properties of these materials also provides directions for the improvement of future generations of ultrafine grain W-based materials.

II. Materials and Methods

A. *Powder Processing and Consolidation*

Nanocrystalline powder with a W to Cr atomic ratio of 10:1 was prepared by milling the appropriate ratio of feedstock powders (99.95% W, -200+325 mesh; 99+% Cr, -325 mesh) in a SPEX 8000 high energy ball mill. For comparison purposes, initially unalloyed W was milled as well. The W and W-Cr powders were milled for up to 20 hours in a hardened steel vial with steel media and a ball-to-powder ratio of 5:2 (20 g of powder). In order to prevent oxidation, milling was conducted in a glovebox kept under an ultra-high purity argon atmosphere. The amount of Fe pickup in the powder due to abrasion of the vial and media was measured using energy dispersive spectroscopy (EDS) in a JEOL 6610LV scanning electron microscope (SEM) operated at 20 kV.

Prior to compaction, the as-milled powder's homogeneity and microstructure were assessed using X-ray diffraction (XRD) and transmission electron microscopy (TEM). The grain size and lattice parameter were calculated from XRD profiles collected using Cu-Kα radiation in a Panalytical X'Pert Pro diffractometer. The grain size was measured from the XRD pattern using a Williamson-Hall analysis of the peak broadening after correcting for instrumental broadening using a NIST LaB_6 standard. The Williamson-Hall method was used in the present work because it has been shown to measure the grain size more accurately than techniques that do not account for microstrain, i.e. the Scherrer equation, which tend to underestimate the grain size.[22] The lattice parameter of the BCC W phase was measured using Rietveld refinement. TEM was used to confirm the XRD grain size. TEM specimens were prepared by mixing the powder in epoxy, manually grinding a powder-epoxy disk until it was less than 10 μm thick, and then argon ion

polishing the disk to electron transparency in a Fischione 1010 ion mill. During ion polishing, the specimen was cooled to 183 K (-90 °C) using a liquid nitrogen cold finger. Bright field TEM micrographs were collected in a JEOL 2010F operating at 200 kV. Individual grains were manually traced and their spherical-equivalent diameters measured.

The milled powders were subsequently consolidated in a Dr. Sinter SPS-515S hot pressing (FAS) apparatus, using various soak times and temperatures to identify the optimal processing parameters for minimizing both porosity and grain growth. Except for samples used subsequently for micropillar compression and Kolsky bar tests, all of the samples were consolidated using an 8 mm diameter graphite punch and die set. The Kolsky bar and micropillar compression specimens were machined from a larger compact consolidated with a 20 mm punch and die set. Both the 8 and 20 mm compacts were consolidated under a uniaxial stress of 100 MPa. During consolidation, the temperature was ramped from room temperature to 843 K (570 °C) in 3 minutes and then from 843 K (570 °C) to the soak temperature at 100 K/min. The soak temperature was systematically varied from 1373 to 1673 K (1100 to 1400 °C) in increments of 100 K, and soak times of 1 and 20 minutes were used at each temperature. During consolidation, the hot zone was held under a vacuum of at least 0.2 mbar. Following consolidation, the temperature in the water-cooled consolidation chamber initially decreased at a rate of ~200 K/min, eventually slowing to <40 K/min after dropping below 1073 K (800 °C). The compacts were rough ground to remove any carbide from their surfaces and sectioned using electro discharge machining (EDM) for microstructural characterization and mechanical testing.

B. *Microstructural Characterization*

The porosity, volume fraction of phases present, and mean grain size of the W-rich BCC phase were quantified in as-compacted samples using standard stereological techniques. A section of each compact was mounted, ground, and polished prior to collecting SEM images for stereological measurements. Metallographic preparation concluded with a suspension of colloidal silica in dilute chromic acid (0.03 M) to enhance grain boundary relief. The micrographs used for grain size measurements were taken in secondary electron mode, whereas those used for volume fraction and porosity measurements were taken in backscatter electron mode. The volume fraction of intermetallic was manually measured using the point counting technique described in ASTM standard E562-11.[23] The porosity was measured following the image analysis procedure outlined in ASTM E1245-03.[24] The mean grain size was measured in accordance with the circular intercept procedure for specimens containing two phases as described in ASTM standard E112-12.[25]

To validate the stereological porosity measurements, the compacts' relative densities were also estimated. Their specific gravities were measured using the Archimedes method in deionized water. Each sample's specific gravity was measured five times giving a relative uncertainty of 0.5 %. The compacts' theoretical densities were calculated by summing the product of each phase's theoretical density and stereological volume fraction.

C. *Mechanical Testing*

Microhardness was measured using a Leco DM-400FT Microhardness Tester with a 1 kg load and a 15 s hold time. Compact as well as individual phase mechanical properties were measured by instrumented nanoindentation using a MTS Nanoindenter XP with a diamond Berkovich tip. The tip's area function was calibrated on a fused silica standard. Indentations were performed at a nominal strain rate of 0.05 s^{-1} to a maximum depth of 1 μm. The hardness and reduced modulus were calculated from the load-displacement data using the Oliver-Pharr method.[26] The Young's modulus was then calculated using standard values for the elastic properties of diamond and the Poisson's ratio of W (ν_W = 0.28).[27]

Select specimens were subjected to additional small scale mechanical testing. After polishing the sample's surface, micropillars with diameter and length of 5 and 10 μm, respectively, were fabricated using the lathe technique in a FEI Nova 600i dual-beam focused ion beam.[28] The micropillars were compressed in the same MTS Nanoindenter XP with a square, 30 x 30 μm flat punch diamond tip. The loading rates in the load-controlled nanoindenter were prescribed to provide nominal strain rates of ~10^{-4} s^{-1}. Engineering stress and strain for each test were calculated from the applied load and cross-head displacement data collected by the nanoindenter. In addition, the samples were observed post-mortem using an SEM.

High strain rate uniaxial compression experiments were conducted on select samples using a 3/8 inch diameter maraging steel Kolsky bar system. Details of a comparable

experimental setup can be found in Reference [29]. For these experiments, cuboidal samples were cut from the bulk materials using a wire EDM and polished to a cross sectional geometry of 2.2 x 2.2 mm and lengths from 1.8-2 mm. Impedance-matched tungsten carbide platens were used to protect the ends of the bars due to the test specimens' high strengths. In addition, Cu pulse shapers were used to produce ramped loading conditions in order to ensure stress equilibrium was achieved within the sample prior to failure. Several specimens were recorded during loading using an Imacon 200 high speed camera. The specimens were illuminated by a Photogenic Powerlight 2500DR flash, and the images were captured with a 2 μs exposure time at a framing rate of 2.2 μs.

III. Powder Characterization

Abrasive wear of the steel vial and media during milling was the source of iron in the present alloys; milling changed the average stoichiometry of the $W_{90}Cr_{10}$ and W powders to $W_{84.1}Cr_{7.1}Fe_{8.8}$ and $W_{90.5}Fe_{9.5}$, as measured by EDS. The two alloys are referred to as W-7Cr-9Fe and W-9Fe for simplicity. Previous studies on mechanical alloying of W reported similar Fe pickup and so this was expected.[30] Here, the addition of Fe modified the equilibrium phases present at the soak temperatures used. Inspection of the ternary W-Cr-Fe phase diagram shows that W and W-10Cr lie in a single-phase, BCC solid solution field at temperatures greater than 1373 K (1100 °C); W-7Cr-9Fe and W-9Fe alloys lie in a two-phase field linking the BCC solid solution with a μ-phase intermetallic.[31] The intermetallic μ-phase precipitated during consolidation.

XRD patterns of the feedstock W-10Cr powder and the W-7Cr-9Fe powder milled for 10 and 20 hours are shown in Figure 1a. The elemental W and Cr powders diffract differentiable sets of BCC Bragg peaks. With increasing time milled, the Cr peaks disappear, while the W peaks broaden due to grain refinement and shift to higher 2θ indicating a change in lattice parameter. The disappearance of the Cr peaks and the change in W's lattice parameter suggest that the W, Cr, and Fe form a metastable solid solution, in line with previous reports on mechanically alloyed W-Cr and W-Fe couples.[32,33] Similarly to the W-7Cr-9Fe powder, the W lattice parameter in the initially pure W powder changes as Fe dissolves into the W lattice.

Figure 1b shows the change in the W-rich solid solution lattice parameter and grain size with time milled for the W-7Cr-9Fe and W-9Fe powders. The evolution in both powders' micro strain, as measured using the Williamson-Hall method, is in agreement with that previously reported by Wagner *et al.* for mechanically milled W, plateauing after 10 hrs of milling at ~0.8 %.[34] Both samples' rate of grain size reduction slowed after 10 hrs of milling; however, their lattice parameters, indicators of the powder's chemical homogeneity, only started to change appreciably after 10 hrs of milling. 20 hrs of milling was chosen as a suitable compromise between achieving a terminal grain size, chemically homogenizing the powder, and avoiding excessive Fe pickup. The mean grain sizes of the 20 hr milled W-7Cr-9Fe and W-9Fe powders were 17±5 and 15±5 nm, as measured using TEM (Figure 2). These values were validated by the XRD measurements of grain size by the Williamson-Hall method (Figure 1b). The as-milled

powders' grain sizes are in line with what has been reported in other studies of high energy ball milled W (~5 to 15 nm).[34–38]

IV. Compaction and Compact Microstructure

Punch displacements measured during some typical consolidation runs with both alloys are shown in Figure 3. The curves were collected while ramping from 843 to 1673 K (570 to 1400 °C) at 100 K/s under a compaction pressure of 100 MPa. The onset of significant punch displacement at around 1173 K (900 °C) indicates that both alloys are beginning to densify, and the densification accelerates before slowing at ~1448 K (1175 °C) where, presumably, full density is being approached. Although both alloys densify over the same temperature range, the Cr-free alloy appears to densify more rapidly at lower temperatures than the Cr-bearing alloy.

The trends in the punch displacement data noted above agree with the stereological porosity versus soak temperature curves presented in Figure 4. As expected, the samples consolidated at soak temperatures of 1473 K (1200 °C) or higher all had less than 2 vol% porosity and so were nearly full density. In addition, the W-9Fe alloy densified more rapidly at lower temperatures. Each compact's specific gravity, porosity measured using stereology, and porosity calculated from its relative density are shown in Table 1. For clarity, the two measures of porosity are presented in adjacent columns; the agreement is good.

Although Figure 4 shows that the samples compacted at 1373 K (1100 °C) for 20 minutes had porosities equivalent to those of samples consolidated at higher temperatures, we found that they were relatively friable and not well bonded at interparticle interfaces. In light of this, 1473 K (1200 °C) at 1 minute was identified as the combination of time and temperature that minimized the thermal excursion while still achieving near full relative density and good interparticle bonding.

Rapid, low temperature densification comparable to that reported above has been previously observed in two other studies of ball milled W and W alloys.[13,39] Oda and coworkers ball milled pure W powder and subsequently FAS consolidated the as-milled powder to near full density at 1273 K (1000 °C) and 50 MPa for 30 minutes.[13] Oda *et al.* did not assess the extent of Fe pickup after milling; however, in an independent W-Fe mechanical alloying study that used milling equipment similar to Oda *et al.*'s, Herr and Samwer observed that the Fe pickup increased linearly with milling time and reached ~70 at% after 80 hrs of milling whenever there was less than 70 at% Fe in the starting charge.[40] Thus, after accounting for the difference in ball to powder ratio used in the two studies, we estimate that there might be as much as perhaps ~20 at% Fe in the powders made by Oda *et al.* after milling for 100 hrs. In addition, Xiang *et al*. mechanically alloyed a mixture of W, Ni, and Fe (W-7Ni-3Fe wt%) powders that they consolidated to 95% relative density using the same pressure, 50 MPa, but holding for only 8 minutes at a higher temperature, 1473 K (1200 °C).[39] The present results are in line with these other reports, although we achieve higher relative densities than Xiang et al. and use a significantly shorter soak time than Oda *et al.*

The μ-phase intermetallic precipitated during consolidation and was present in all of the compacts along with the majority BCC solid solution phase. EDS was performed on the samples consolidated at 1673 K (1400 °C) for 20 minutes to determine both phases' compositions. In the W-7Cr-9Fe samples, the intermetallic and BCC phases had respective stoichiometries of $W_{46}Cr_{16}Fe_{38}$ and $W_{92}Cr_3Fe_5$, whereas in the W-9Fe compacts, the same phases had compositions of $W_{50}Fe_{50}$ and $W_{98}Fe_2$. In addition, we performed nanoindentation on the intermetallic in these samples to measure its hardness, which was determined to be about 17.4 GPa averaging over 8 indents.

There was a larger volume fraction of the μ-phase in the Cr-bearing samples, but both alloys' compacts had qualitatively similar microstructures: regions of the W-rich, BCC solid solution phase containing many individual grains were interspersed with intermetallic precipitates as demonstrated by the micrographs in Figure 5. For soak temperatures greater than 1373 K (1100 °C), the volume fraction of the μ-phase that precipitated during compaction was, within error, equal to that predicted by the equilibrium phase diagram (as assessed by THERMOCALC software) given the alloys' stoichiometries (Figure 6).[41] For the samples consolidated at 1373 K (1100 °C), the intermetallic volume fraction was greater than 10% but could not be more accurately measured because of difficulties resolving the two phases. The residual porosity, also evident in the micrographs in Figure 5, was located predominantly at triple junctions in the W-rich, BCC solid solution phase, the intermetallic-BCC phase boundaries, and the centers of larger regions of intermetallic. The samples consolidated at 1673 K (1400 °C)

for 20 minutes shown in Figure 5 had the coarsest microstructures of all of the compacts, and most of the other samples had similar microstructures, albeit on a finer length-scale. In the samples consolidated at 1373 K (1100 °C) for 1 minute, individual powder particles were separated by pockets of porosity and could be clearly delineated.

The compacts' grain sizes (D) are plotted against their soak temperatures in Figure 7. Even at the lowest soak temperature and shortest hold time (1373 K (1100 °C) for 1 min), the grain size in both alloys was considerably larger than for the as-milled powder. The observed onset of grain growth at temperatures below 1373 K (1100 °C) is in agreement with past reports of grain boundary migration in heavily worked W alloys.[4,5] In a study of warm-drawn, K-doped W wire, for example, Meieran and Thomas observed grain boundary migration at temperatures as low as 1173 K (900 °C).[5] In our samples, the grain boundaries are sufficiently mobile by 1673 K (1400 °C) that the grains rapidly coarsen to micron dimensions.

It is also evident from the results in Figure 7 that Cr supports a finer grain structure in the W-7Cr-9Fe samples relative to the W-9Fe samples. Cr appears to slow grain growth most at the lower soak temperatures. For example, the W-7Cr-9Fe samples consolidated at 1373 K (1100 °C) for 1 and 20 minutes have 50% smaller mean linear intercept grain sizes than the similarly processed W-9Fe samples, whereas by 1673 K (1400 °C), the W-7Cr-9Fe and W-9Fe samples have effectively the same grain size. Additionally, one prior study of Cr-doped W reported that a W-30Cr alloy compact had a ~5x smaller grain size than similarly processed pure W compacts after sintering.[32] The Cr can inhibit grain

growth in two ways. First, Cr is expected to segregate to grain boundaries in W and thereby lower the driving force for grain growth as well as the grain boundary mobility; this is specifically the case at 1373 K (1100 °C).[42] Second, if the μ-phase exerts a pinning force on mobile grain boundaries in the W-rich, BCC phase, the larger volume fraction of μ-phase in the Cr-bearing sample would result in more sluggish grain growth.

From a practical perspective, it is of interest that the grain growth kinetics are sufficiently slow in the Cr-bearing sample that the powders can be consolidated at 1473 K (1200 °C) for 1 minute to near full density and still retain ultrafine grains (D ~130 nm). These samples are therefore singled out for the micropillar compression and Kolsky bar experiments described later. We include additional low- and high-magnification SEM micrographs of this material in Figure 8 to illustrate the distribution of the intermetallic, the porosity, and the refined grain structure.

V. Mechanical Properties

A. *Strengthening Contributions*

Consistent with other reports of grain-size strengthening in W and W alloys, the compacts' microhardnesses conform to a Hall-Petch scaling, as shown in Figure 9. For comparison purposes, the data collected in this study are plotted alongside microhardness measurements on nominally pure W compacts fabricated by hot isostatic pressing W nanopowders from Reference [20]. Numerical values for the Hall-Petch slopes are shown in the figure, and the extrapolation of the trend to infinite grain size is shown at the y-intercept. The slopes are similar among the three alloys, and the y-intercepts

suggest that the W-7Cr-9Fe and W-9Fe compacts are respectively about 1.6 and 1.0 GPa harder than a nominally pure W compact, independently of grain size effects.

One possible explanation for the higher hardness of the Fe- and Cr- bearing alloys is classical solid solution strengthening of the BCC W-rich phase. We estimate solid solution hardening using the Fleischer equation:

$$\Delta H = 3^{3/2}\frac{G_W c^{1/2}}{700}\left|\frac{\frac{1}{G_W}\frac{dG}{dc}}{1+\frac{1}{2G_W}\left|\frac{dG}{dc}\right|}-\frac{3}{a}\frac{da}{dc}\right|^{3/2} \qquad (1)$$

where the $3^{3/2}$ prefactor is used to convert shear stress to hardness, G_W is W's shear modulus, G is the alloy's shear modulus, a is the lattice parameter, and c is the solute concentration.[43] If we assume that there are no solute-solute interactions so that the strengthening effects of Fe and Cr are additive, then using the solute concentrations given earlier and the material properties listed in References [44] and [45], we estimate that solid solution strengthening would increase the hardness in both the W-7Cr-9Fe and W-9Fe compacts by ~20 MPa relative to a nominally pure W compact. The solid solution strengthening contribution is thus two orders of magnitude too small to explain the >1 GPa hardening seen in the present alloys. Although solid solution strengthening effects have been found to be dramatically enhanced in extremely fine grain nanomaterials,[46] the grain sizes in the present alloys are too big to permit such an explanation here.

A more likely explanation for the high hardnesses of our alloys relative to pure W is the presence of the hard intermetallic μ-phase. This intermetallic's hardness (~17 GPa) is

much higher than that of even the hardest nominally pure W compacts from the study of Vashi et al. in Figure 9 (~13 GPa). Its presence at volume fractions up to 20% can adequately explain the alloy hardness; using the model of Gurland and Lee[47] we can estimate the hardening factor as:

$$\Delta H = (H_{\mu} - H_{W}) f_{IM} C_{IM} \qquad (2)$$

where H_{μ} is the intermetallic's hardness, H_W is the hardness of pure W, f_{IM} is the volume fraction of the intermetallic (equal to 14 and 20% in the W-9Fe and W-7Cr-9Fe alloys, respectively), and C_{IM} is a contiguity parameter for the intermetallic (defined in Reference [48] and estimated as $C_{IM} \approx 0.6$ based on its volume fraction and the random, homogeneous, and isotropic microstructure).[49] Using the y-intercept from Vashi *et al.*'s data, i.e., $H_W = 3.7$ GPa, the ΔH values for the W-7Cr-9Fe and W-9Fe compacts are 1.6 and 1.2 GPa, respectively. These align with the measured values of 1.6 and 1.0 reasonably well. We conclude that the alloy compacts are clearly substantially strengthened because of grain size refinement (cf. Figure 9), but with a non-negligible contribution from the presence of the intermetallic.

B. *Micropillar Compression*

Micropillar compression tests were used to measure the yield strength and study the deformation behavior of the ultrafine grain BCC phase. We therefore made efforts to avoid larger μ-phase precipitates and pores when machining the microcompression pillars, but cannot rule out the possible presence of some μ-phase content in them. Engineering stress-strain curves from several microcompression experiments are shown in Figure 10. The Young's modulus, taken from a linear fit of the elastic region of the

stress-strain curve, was ~50% of the nanoindentation value (~355 GPa). This difference is ascribed to the compliance of the pillar's base and a non-zero angle (< 1°) between the pillar's longitudinal axis and the platen's face normal.[50] Although micropillar compression experiments are generally not well suited for accurate measurement of the Young's modulus, the engineering stress and yield strength values can be reliably measured. The average 0.2% offset yield strength was 5.15 GPa, with apparent hardening to an ultimate engineering stress of about 6 GPa followed by a plateau in the stress-strain response. The plateau is associated with the development of a single shear band within the pillar. An example of a shear offset, captured just before failure at an applied stress level of 6.3 GPa, is shown in the inset of Figure 10.

We are not aware of any other reports on the micropillar compression testing of ultrafine grain W, but our pillars are large (~5x10 μm) compared to the grain size (0.13 μm) and can thus be compared to bulk compression tests. It is particularly instructive to highlight two differences between our results and those from quasi-static compression tests on bulk coarse and ultrafine grain W specimens. First, the pillars' average yield strength of 5.15 GPa is substantially higher than the 3.1 GPa yield strength exhibited by a high pressure torsion specimen reported by Wei *et al.*[7] This increment in strength is most likely due to better alignment of our specimen with the loading axis, as the high pressure torsion specimen had a similar grain size (170 nm) and microhardness (11 GPa), and Wei *et al.* reported issues with specimen misalignment and buckling during loading.[7] Second, the shear localization observed in our micropillar compression specimens is consistent with another recent report by Butler *et al.* of shear localization during quasi-static compression

testing of bulk ultrafine grained $W_{1-x}Re_x$ (x = 5, 10, 25 at%) compacts.[51] These W-Re compacts were also synthesized by powder processing and had porosities similar to our Kolsky bar specimens', but had slightly larger grain sizes (200 to 350 nm). Although Butler *et al.*'s W-Re samples exhibited lower yield strengths than ours, their post-mortem analysis of the compression specimens showed evidence of shear localization.

Apart from the work by Butler *et al.* described above, W test specimens with grain sizes ranging from 50 μm to 170 nm were reported to have only deformed by homogeneous plastic deformation and axial cracking along grain boundaries;[7,10,52] the only other reports of shear localization in W were from high strain rate tests of ultrafine grain specimens.[6,7,10,11,53] In such high strain rate tests, the shear localization has been most commonly attributed to adiabatic heating that causes localized softening on planes of maximum shear stress. The low strain rates used in both Butler *et al.*'s and our quasi-static tests are not consistent with this kind of adiabatic shear localization, and instead argue for a structural origin of shear softening. This more closely resembles that seen during quasi-static compression testing of ultrafine grain Fe,[54] Ta,[55] and Fe-10Cu.[56] In these other materials, shear localization occurs because grain rotation leads to geometric softening.[57,58]

C. *High Strain Rate Deformation*

A representative engineering stress versus time curve from a Kolsky bar test conducted at a strain rate of 600 s^{-1} is shown in Figure 11. Note that engineering strain values are not reported because these specimens failed at very low strains, which are difficult to

measure accurately with a Kolsky bar system. The specimen was loaded until failure, followed by rapid unloading. Accompanying the stress-time curve are images collected using high-speed videography, which serve to illustrate the specimen's brittle mode of failure at 76 μs. The average failure stress was 4.14 GPa, which is in rough agreement with the Tabor estimate based on the measured microhardness value reported earlier ($\sigma \approx H/3 = 13.5 / 3$ GPa = 4.5 GPa).

Coarse-grained W strained at high rates deforms by a combination of homogeneous plastic deformation and axial cracking,[52] and ultrafine grain W has been reported to exhibit adiabatic shear localization.[6,7,10,11,53] In our samples, the residual pores act as stress risers and crack nucleation sites, while the brittle intermetallic μ-phase lowers the compact's toughness. Together, these two microstructural features likely contributed to the onset of fracture events at high rates. Based on our samples' grain size and the micropillar compression results on the W-rich BCC phase reported in the previous section, we speculate that the BCC phase would favor shear localization under both quasi-static *and* high strain rate testing. This is because other ultrafine grain BCC metals that exhibit structural shear localization during quasi-static compression tests also typically exhibit shear localization in high strain rate tests.[54] Therefore it is expected that further tuning of the alloy composition and consolidation schedule to reduce the volume fraction of the intermetallic and the porosity could permit some tuning of the propensity for shear localization versus cracking.

VI. Conclusions

Ultrafine grain W-rich alloy (W-9Fe and W-7Cr-9Fe) powders have been synthesized via mechanical alloying, and the microstructure and mechanical properties of compacts made from the powder systematically investigated. The main results of this work are as follows:

Ultrafine grain W-rich compacts with high relative densities were achieved by suppressing the rate of grain growth during consolidation, by (1) minimizing the thermal excursion during consolidation, thereby slowing thermally activated grain growth, and (2) alloying with Cr, an element expected to reduce grain boundary energy and mobility in W. Dense compacts with grain sizes as small as 130 nm were synthesized.

The ultrafine grain compacts' hardnesses were greater than 12 GPa due to grain size strengthening in the W-rich, BCC phase, and followed the Hall-Petch scaling. A second significant contribution to their hardnesses (~1-2 GPa) came from the hard intermetallic μ-phase that precipitated during compaction.

The ultrafine grain compacts exhibited very high quasi-static and dynamic compressive failure strengths measured using micropillar compression and Kolsky bar tests, respectively. During micropillar compression experiments, pillars that were ion-milled out of a compact began to yield at 5 GPa and eventually failed by shear localization upon loading to 6 GPa. During Kolsky bar tests on bulk specimens

machined out of the same compacts, the samples failed at an average stress of 4.14 GPa.

Acknowledgements—This study was supported by the US Defense Threat Reduction Agency under Grant No. HDTRA1-11-1-0062. ZCC acknowledges support from the Department of Defense through the NDSEG fellowship program. ELH acknowledges support from the US Army Research Laboratory through the Oak Ridge Institute for Space and Education (ORISE) program # 1120-1120-99. BES would like to acknowledge support work at the from the Cooperative Research and Development Agreement #11-24. We would like to thank Ms. Alexandria Will-Cole for her indentation work on the intermetallic phase, Dr. Kisub Cho for performing the THERMOCALC calculations, and Dr. Daniel T. Casem for his assistance with the Kolsky bar tests.

[1] B.E. Schuster, J.P. Ligda, Z.L. Pan, and Q. Wei: *JOM*, 2011, vol. 63, pp. 27–31.

[2] Q. Wei, K.T. Ramesh, B.E. Schuster, L.J. Kecskes, and R.J. Dowding: *JOM*, 2006, vol. 58, pp. 40–44.

[3] D.B. Snow: *Metall. Trans. A*, 1976, vol. 7, pp. 783–94.

[4] D.B. Snow: *Metall. Trans. A*, 1979, vol. 10, pp. 815–21.

[5] E.S. Meieran and D.A. Thomas: *Trans Met Soc AIME*, 1965, vol. 233, pp. 937–43.

[6] L.J. Kecskes, K.C. Cho, R.J. Dowding, B.E. Schuster, R.Z. Valiev, and Q. Wei: *Mater. Sci. Eng. A*, 2007, vol. 467, pp. 33–43.

[7] Q. Wei, H.T. Zhang, B.E. Schuster, K.T. Ramesh, R.Z. Valiev, L.J. Kecskes, R.J. Dowding, L.S. Magness Jr., and K. Cho: *Acta Mater.*, 2006, vol. 54, pp. 4079–89.

[8] A.P. Zhilyaev and T.G. Langdon: *Prog. Mater. Sci.*, 2008, vol. 53, pp. 893–979.

[9] L.S. Magness Jr.: *Mech. Mater.*, 1994, vol. 17, pp. 147–54.

[10] Q. Wei, L.J. Kecskes, and K.T. Ramesh: *Mater. Sci. Eng. A*, 2013, vol. 578, pp. 394–401.

[11] Q. Wei, T. Jiao, K.T. Ramesh, E. Ma, L.J. Kecskes, L. Magness, R. Dowding, V.U. Kazykhanov, and R.Z. Valiev: *Acta Mater.*, 2006, vol. 54, pp. 77–87.

[12] A.K. Srivastav and B.S. Murty: *J. Alloys Compd.*, 2012, vol. 536, Supplement 1, pp. S41–S44.

[13] E. Oda, K. Ameyama, and S. Yamaguchi: *Mater. Sci. Forum*, 2006, vol. 503-504, pp. 573–78.

[14] H. Wang, Z.Z. Fang, K.S. Hwang, H. Zhang, and D. Siddle: *Int. J. Refract. Met. Hard Mater.*, 2010, vol. 28, pp. 312–16.

[15] R. Sarkar, P. Ghosal, M. Premkumar, A.K. Singh, K. Muraleedharan, A. Chakraborti, T.P. Bagchi, and B. Sarma: *Powder Metall.*, 2008, vol. 51, pp. 166–70.

[16] T.S. Srivatsan, K. Manigandan, M. Petraroli, R.M. Trejo, and T.S. Sudarshan: *Adv. Powder Technol.*, 2013, vol. 24, pp. 190–99.

[17] B.R. Klotz, F.R. Kellogg, E.M. Klier, R.J. Dowding, and K.C. Cho: *Characterization, Processing, and Consolidation of Nanoscale Tungsten Powder*, 2009.

[18] K.C. Cho, R.H. Woodman, B.R. Klotz, and R.J. Dowding: *Mater. Manuf. Process.*, 2004, vol. 19, pp. 619–30.

[19] O. El-Atwani, D.V. Quach, M. Efe, P.R. Cantwell, B. Heim, B. Schultz, E.A. Stach, J.R. Groza, and J.P. Allain: *Mater. Sci. Eng. A*, 2011, vol. 528, pp. 5670–77.

[20] U.K. Vashi, R.W. Armstrong, and G.E. Zima: *Metall. Trans.*, 1970, vol. 1, pp. 1769–71.

[21] C. Agte and J. Vacek: *Tungsten and Molybdenum*, NASA Trans., 1963.

[22] H.H. Tian and M. Atzmon: *Philos. Mag. A*, 1999, vol. 79, pp. 1769–86.

[23] ASTM Standard E562-11: *Test Method for Determining Volume Fraction by Systematic Manual Point Count*, vol. 03.01, Annual Book of ASTM Standards, 2011.

[24] ASTM Standard E1245-03: *Practice for Determining the Inclusion or Second-Phase Constituent Content of Metals by Automatic Image Analysis*, vol. 03.01, Annual Book of ASTM Standards, 2008.

[25] ASTM Standard E112-12: *Test Methods for Determining Average Grain Size*, vol. 03.01, Annual Book of ASTM Standards, 2012.

[26] W.C. Oliver and G.M. Pharr: *J. Mater. Res.*, 2004, vol. 19, pp. 3–20.

[27] ASM Handbook: Vol. 2 - Properties and Selection: Nonferrous Alloys and Special Purpose Materials, ASM International, Metals Park, OH, 1990.

[28] M.D. Uchic, D.M. Dimiduk, J.N. Florando, and W.D. Nix: *Science*, 2004, vol. 305, pp. 986–89.

[29] W.W. Chen and B. Song: *Split Hopkinson (Kolsky) Bar Design, Testing and Applications*, Springer, New York, NY, 2011.

[30] T.H. Courtney and Z. Wang: *Scr. Metall. Mater.*, 1992, vol. 27, pp. 777–82.

[31] P. Gustafson: *Metall. Trans. A*, 1988, vol. 19, pp. 2531–46.

[32] S. Telu, A. Patra, M. Sankaranarayana, R. Mitra, and S.K. Pabi: *Int. J. Refract. Met. Hard Mater.*, 2013, vol. 36, pp. 191–203.

[33] M.S. El-Eskandarany, K. Sumiyama, and K. Suzuki: *Acta Mater.*, 1997, vol. 45, pp. 1175–87.

[34] C.N.J. Wagner, E. Yang, and M.S. Boldrick: *Nanostructured Mater.*, 1996, vol. 7, pp. 1–11.

[35] H.J. Fecht, E. Hellstern, Z. Fu, and W.L. Johnson: *Metall. Trans. A*, 1990, vol. 21, pp. 2333–37.

[36] R. Malewar, K.S. Kumar, B.S. Murty, B. Sarma, and S.K. Pabi: *J. Mater. Res.*, 2007, vol. 22, pp. 1200–1206.

[37] A.O. Aning, Z. Wang, and T.H. Courtney: *Acta Metall. Mater.*, 1993, vol. 41, pp. 165–74.

[38] D. Oleszak and P.H. Shingu: *J. Appl. Phys.*, 1996, vol. 79, pp. 2975–80.

[39] D.P. Xiang, L. Ding, Y.Y. Li, J.B. Li, X.Q. Li, and C. Li: *Mater. Sci. Eng. A*, 2012, vol. 551, pp. 95–99.

[40] U. Herr and K. Samwer: *Nanostructured Mater.*, 1992, vol. 1, pp. 515–21.

[41] J.O. Andersson, T. Helander, L. Höglund, P. Shi, and B. Sundman: *Calphad*, 2002, vol. 26, pp. 273–312.

[42] T. Chookajorn, H.A. Murdoch, and C.A. Schuh: *Science*, 2012, vol. 337, pp. 951–54.

[43] D. Peckner: *The Strengthening of Metals*, Reinhold Pub. Corp., 1964, pp. 93–139.

[44] R.W. Hertzberg: *Deformation and Fracture Mechanics of Engineering Materials*, 3rd ed., Wiley, New York, NY, 1996, pp. 8.

[45] C.S. Barrett and T.B. Massalski: *Structure of Metals*, 3rd ed., McGraw-Hill, New York, NY, 1966, pp. 626–31.

[46] T.J. Rupert, J.C. Trenkle, and C.A. Schuh: *Acta Mater.*, 2011, vol. 59, pp. 1619–31.

[47] H.C. Lee and J. Gurland: *Mater. Sci. Eng.*, 1978, vol. 33, pp. 125–33.

[48] E. Underwood: *Quantitative Stereology*, Addison-Wesley Publishing Co., Reading, MA, 1970, pp. 99-103.

[49] Z. Fan, A. P. Miodownik, and P. Tsakiropoulos: *Mater. Sci. Technol.*, 1993, vol. 9, pp. 1094–1100.

[50] H. Zhang, B.E. Schuster, Q. Wei, and K.T. Ramesh: *Scr. Mater.*, 2006, vol. 54, pp. 181–86.

[51] B. Butler, E. Klier, D. Casem, A. Dwivedi, M. Gallagher, and J. Hays: *Demonstration of Shear Localization in Ultrafine Grained Tungsten Alloys via Powder Metallurgy Processing Route*, Army Research Laboratory, 2012.

[52] A.M. Lennon and K.T. Ramesh: *Mater. Sci. Eng. A*, 2000, vol. 276, pp. 9–21.

[53] Q. Wei, K.T. Ramesh, E. Ma, L.J. Kesckes, R.J. Dowding, V.U. Kazykhanov, and R.Z. Valiev: *Appl. Phys. Lett.*, 2005, vol. 86, pp. 101907–101907–3.

[54] D. Jia, K.T. Ramesh, and E. Ma: *Acta Mater.*, 2003, vol. 51, pp. 3495–3509.

[55] J.P. Ligda, B.E. Schuster, and Q. Wei: *Scr. Mater.*, 2012, vol. 67, pp. 253–56.

[56] J.E. Carsley, A. Fisher, W.W. Milligan, and E.C. Aifantis: *Metall. Mater. Trans. A*, 1998, vol. 29, pp. 2261–71.

[57] S.P. Joshi and K.T. Ramesh: *Acta Mater.*, 2008, vol. 56, pp. 282–91.

[58] S.P. Joshi and K.T. Ramesh: *Mater. Sci. Eng. A*, 2008, vol. 493, pp. 65–70.

Captions

Fig. 1—a) Set of XRD scans taken from the feedstock and W-7Cr-9Fe powder milled for 10 and 20 hrs. Note the disappearance of the Cr (110) Bragg peak in the highlighted region after 10 hrs of milling. This, along with the change in W lattice parameter, suggests the formation of a solid solution. b) Williamson-Hall and Rietveld analysis give the W-rich BCC phase's grain size and lattice parameter as a function of milling time for both alloys.

Fig. 2—Representative TEM micrographs of the as-milled a) W-7Cr-9Fe and b) W-9Fe powders illustrating the powders' nanocrystalline grain structure. The inset electron diffraction patterns feature the uniform rings characteristic of nanocrystalline materials.

Fig. 3—Punch displacement curves measured during the heating ramp-up phase for the two alloys, under an applied stress of 100 MPa.

Fig. 4—Stereological porosity after compaction experiments at a variety of soak temperatures and two soak times, 1 and 20 minutes.

Table I: Compact properties after densification, including specific gravity, ρ (relative uncertainty: 0.5%), porosity measured using stereology (relative uncertainty: 50%), and porosity calculated from the relative density (relative uncertainty: 20%) for each compact.

Fig. 5—Backscatter electron micrographs of a) W-7Cr-9Fe and b) W-9Fe compacts consolidated at 1673 K (1400 °C) for 20 minutes. These samples had the coarsest microstructures of all the compacts. The μ-phase precipitates in both samples are generally darker than the BCC solid solution due to the lower W content. The precipitates are also distributed randomly throughout the BCC solid solution, which itself is composed of many individual grains. The black dots in both micrographs are residual pores.

Fig. 6—Volume fraction intermetallic predicted by THERMOCALC and measured using stereology for compacts consolidated at temperatures greater than 1373 K (1100 °C). All of the predicted and experimental volume fractions are within 3 vol% of each other, which is reasonable given uncertainties in the global stoichiometry of the powder and the stereology measurements.

Fig. 7—Grain sizes of compacts made from both alloys and consolidated at various soak temperatures and two soak times, 1 and 20 minutes. Also shown for comparison is the grain size of the as-milled powder.

Fig. 8—a) Low- and b) high-magnification secondary electron micrographs of the optimized W-7Cr-9Fe compact consolidated using the 20 mm die at 1473 K (1200 °C) for 1 min. The low-magnification micrograph illustrates the distribution of porosity (black regions) and the μ-phase intermetallic (darker grey contrast). The high-magnification micrograph illustrates this sample's ultrafine grain structure (D ~130 nm).

Fig. 9—Hall-Petch plot for compacts made with both alloys, from samples compacted at various times and temperatures to densities in excess of 98%. Microhardness values from Vashi *et al*. on nominally pure W compacted to 95% relative density are also presented for comparison.[20] According to Vashi *et al*., the hardness of their W specimens was independent of load between loads of 0.2 and 2 kgf, and the data shown is the average of the hardnesses measured using loads of 0.2, 0.3 and 2 kgf. The data point labeled with a star is the hardness of the W-7Cr-9Fe sample consolidated with the 20 mm die.

Fig. 10—Some typical engineering stress-strain curves from micropillar compression tests on pillars preferentially milled from the BCC solid solution phase. Inset shows a shear offset in a micropillar loaded to 6.3 GPa.

Fig. 11—An engineering stress-time curve collected during a Kolsky bar test conducted at a strain rate of 600 s^{-1}. The test specimen was cut from the W-7Cr-9Fe compact consolidated at 1473 K (1200 °C) using the 20 mm die. The accompanying high speed photographs were taken at the times indicated by the lines. The arrows next to the first frame indicate the loading direction, and the test specimen's orientation is the same in all of the photographs.

Table I: Compact properties after densification, including specific gravity, ρ (relative uncertainty: 0.5%), porosity measured using stereology (relative uncertainty: 50%), and porosity calculated from the relative density (relative uncertainty: 20%) for each compact.

Alloy, Die Diameter	Temp. (K (°C))	Time (min.)	ρ (g/cc)	Porosity (%)	$100*(1-\rho/\rho_T)$ (%)
W-9Fe, 8 mm	1373 (1100)	1	17.7	4.5	3.5
		20	18.1	0.5	1.1
	1473 (1200)	1	18.1	0.6	1.1
		20	18.1	0.3	1.4
	1573 (1300)	1	18.1	1	1.3
		20	18.1	0.8	1.4
	1673 (1400)	1	18.1	1	1.4
		20	18.1	1.3	1.5
W-7Cr-9Fe, 8 mm	1373 (1100)	1	16.1	7	8.5
		20	17.3	0.9	1.5
	1473 (1200)	1	17.3	0.5	1.8
		20	17.3	0.8	1.5
	1573 (1300)	1	17.3	1.1	1.5
		20	17.4	0.8	1.2
	1673 (1400)	1	17.5	0.9	0.9
		20	17.6	1	0.6
W-7Cr-9Fe, 20 mm	1473 (1200)	1	17.0	1.7	3.3

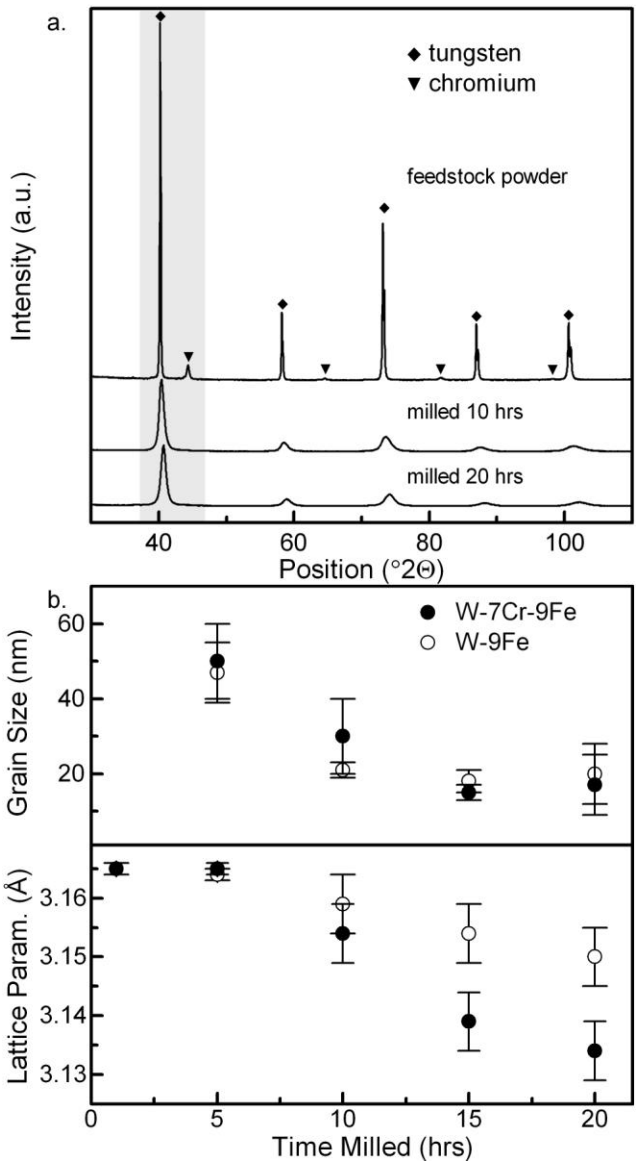
a.
◆ tungsten
▼ chromium
feedstock powder
milled 10 hrs
milled 20 hrs
Intensity (a.u.)
40
60
80
100
Position (°2Θ)
b.
W-7Cr-9Fe
W-9Fe
Grain Size (nm)
60
40
20
Lattice Param. (Å)
3.16
3.15
3.14
3.13
0
5
10
15
20
Time Milled (hrs)

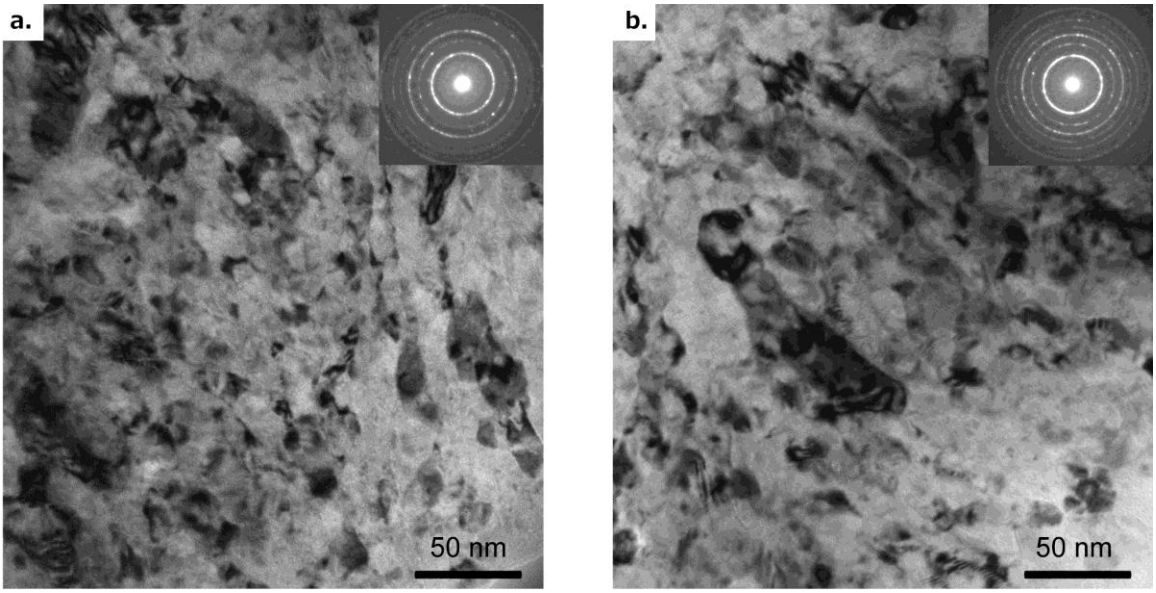
a.
50 nm
b.
50 nm

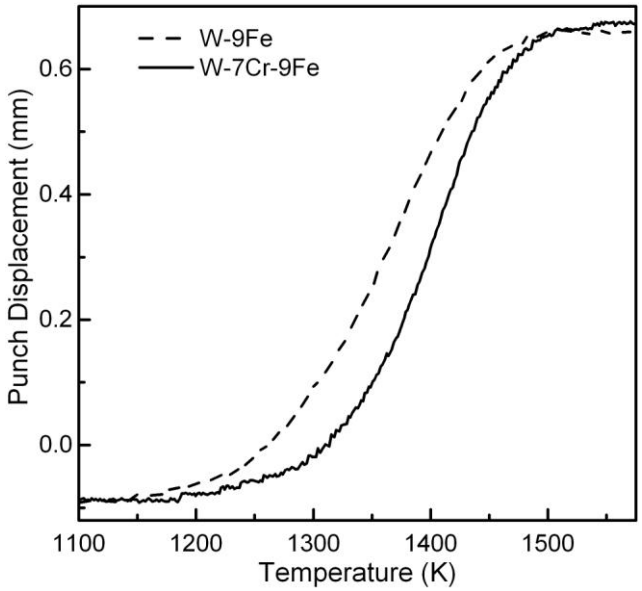
W-9Fe
W-7Cr-9Fe
Punch Displacement (mm)
0.0
0.2
0.4
0.6
1100
1200
1300
1400
1500
Temperature (K)

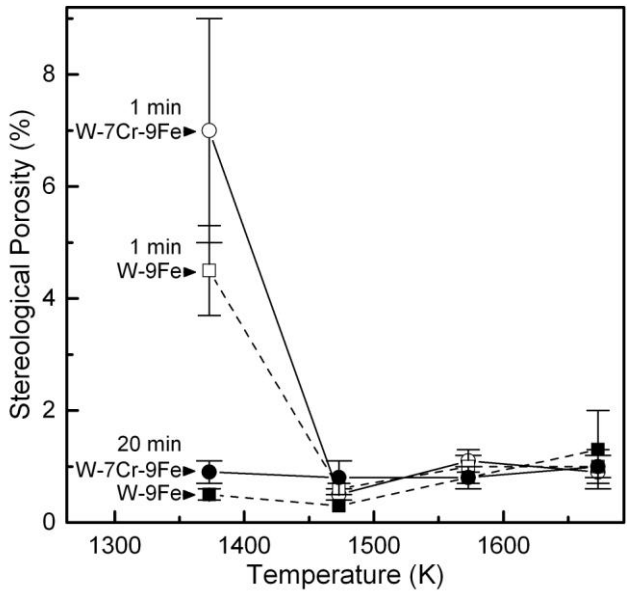
Stereological Porosity (%)
Temperature (K)
1 min
W-7Cr-9Fe
1 min
W-9Fe
20 min
W-7Cr-9Fe
W-9Fe
0
2
4
6
8
1300
1400
1500
1600

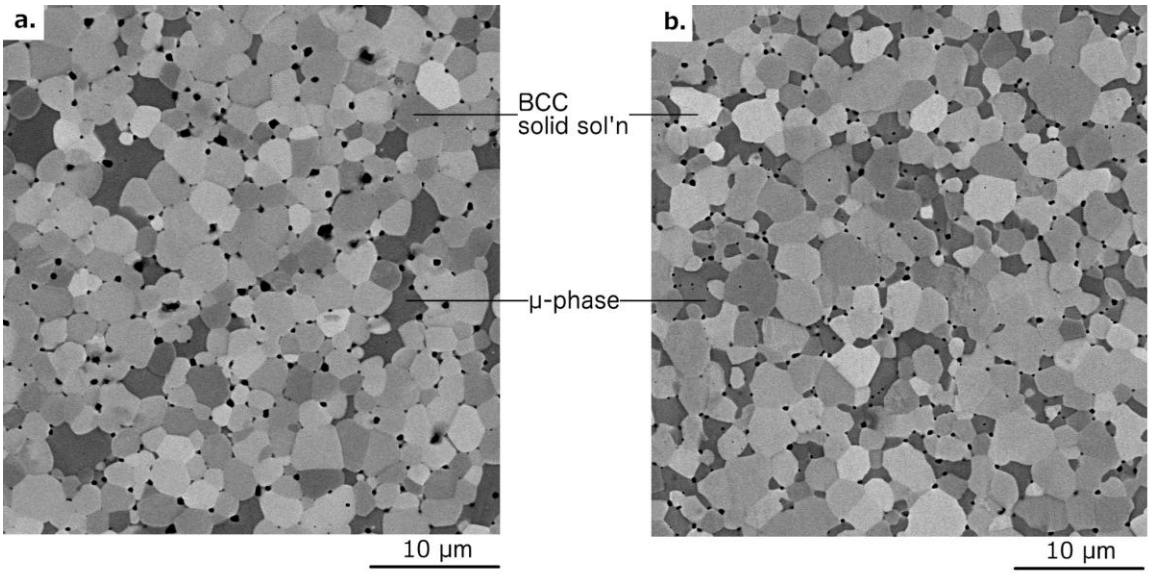
a.
b.
BCC
solid sol'n
μ-phase
10 μm
10 μm

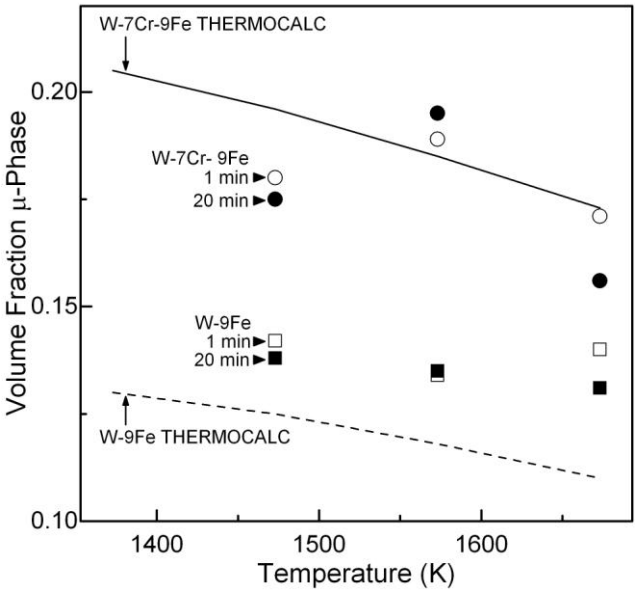
W-7Cr-9Fe THERMOCALC
W-7Cr- 9Fe
1 min
20 min
W-9Fe
1 min
20 min
W-9Fe THERMOCALC
Volume Fraction μ-Phase
Temperature (K)
0.10
0.15
0.20
1400
1500
1600

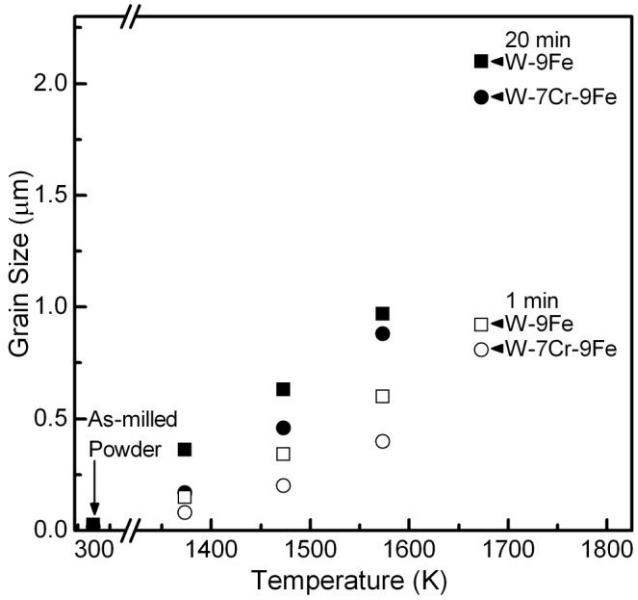
20 min
W-9Fe
W-7Cr-9Fe
1 min
W-9Fe
W-7Cr-9Fe
As-milled
Powder
Grain Size (μm)
Temperature (K)
0.0
0.5
1.0
1.5
2.0
300
1400
1500
1600
1700
1800

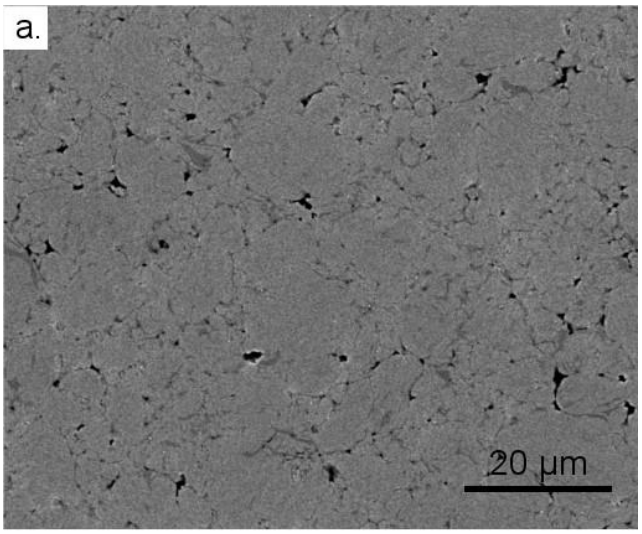
a.
20 μm

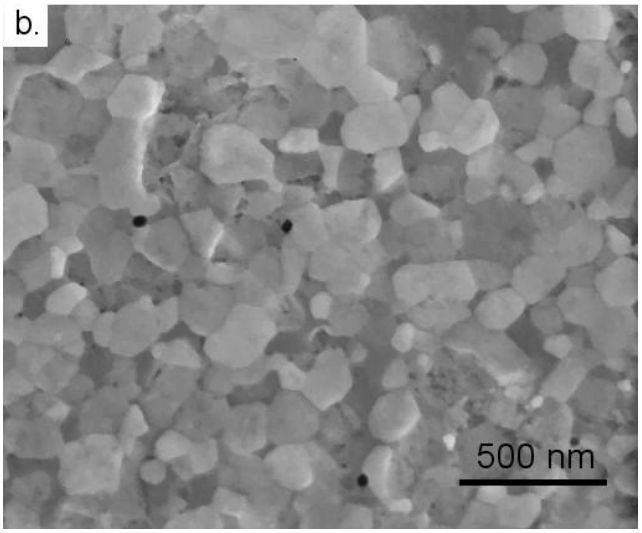
b.
500 nm

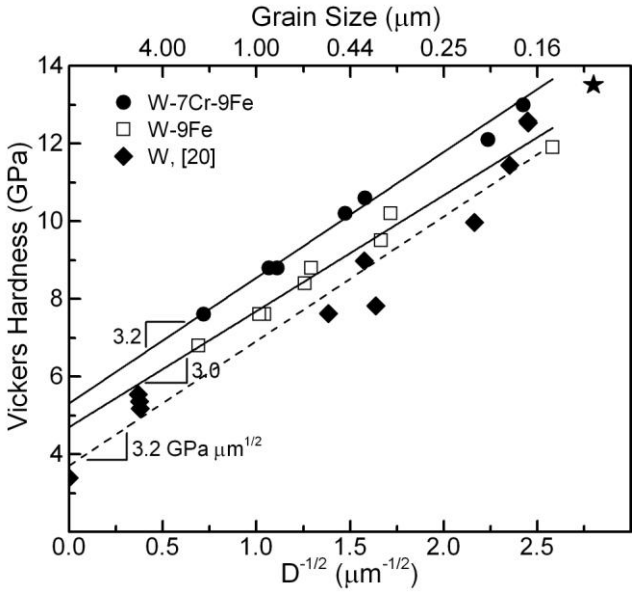
Grain Size (μm)
4.00
1.00
0.44
0.25
0.16
W-7Cr-9Fe
W-9Fe
W, [20]
3.2
3.0
3.2 GPa μm^1/2
Vickers Hardness (GPa)
D^-1/2 (μm^-1/2)

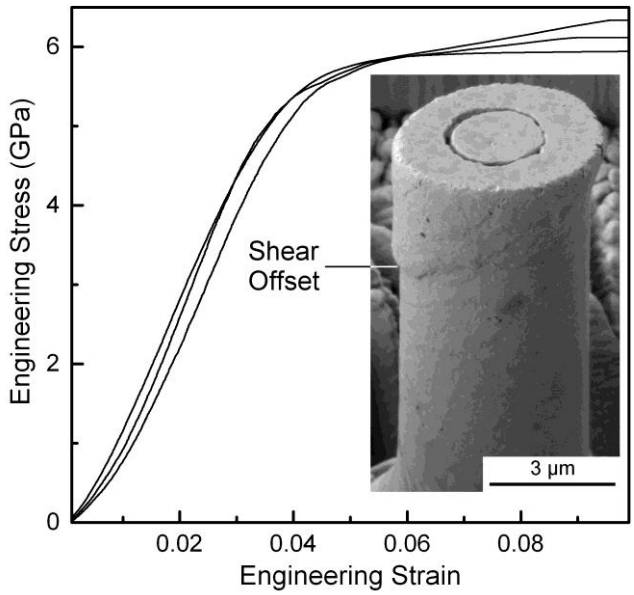
Engineering Stress (GPa)
Engineering Strain
Shear
Offset
3 μm
0
2
4
6
0.02
0.04
0.06
0.08

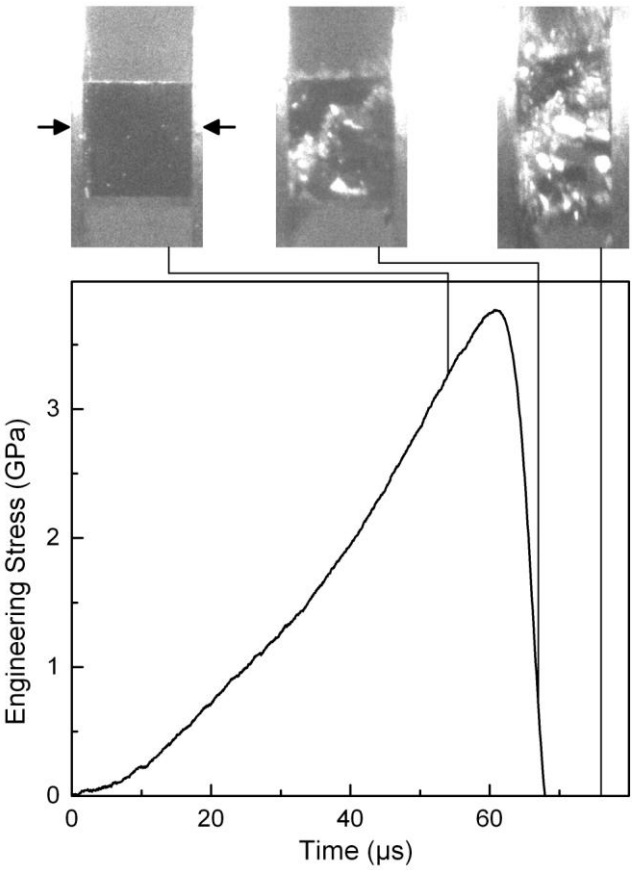
Engineering Stress (GPa)
Time (μs)
0
1
2
3
0
20
40
60